Line Current Ripple Minimization PWM Strategy With Reduced Zero-Sequence Circulating Current for Two Parallel Interleaved Three-Phase Converters

Zhiyong Zeng, *Member, IEEE*, Zhongxi Li, *Student Member, IEEE*, and Stefan M. Goetz, *Member, IEEE*

***Abstract*—This article proposes a line-current ripple minimization pulsewidth modulation strategy with reduced zero-sequence circulating current (ZSCC) for two parallel three-phase two-level converters. We split each 60° sector into six subsectors, each applies the nearest three vectors to ensure minimal line-current ripple. To reduce the ZSCC, we further investigate all vector sequences of the nearest three vectors and derive an optimal vector sequence for each of the six subsectors. We unify all carrier sequences under a carrier-based modulation scheme with the assistance of voltage injections. The injected voltage can be computed by a simple algorithm that allows easy implementation in mainstream microcontrollers. The experimental results validate that the proposed method maintains the minimal line-current ripple while significantly reducing the ZSCC compared to the existing line current ripple minimization methods.**

***Index Terms*—Common mode voltage injections PWM, line current ripple, paralleled interleaved three-phase inverter, root mean square (RMS), zero-sequence-circulating current (ZSCC).**

I. Introduction

THE TWO parallel interleaved three-phase inverters form a popular topology in many different applications, such as large drives, high power renewable energy generation, and uninterruptable power supplies. The two parallel interleaved three-phase two-level converters share a common dc capacitor, and inductors are inserted between two parallel converters to suppress the circulating current, and according to the structure of the inductor adopted, the two parallel converter can be categorized as two types: the coupled inductor (CI) based system [1]–[5], and common-mode inductor (CMI)-based system [6]–[15].

CI inductor suppresses the circulating current across the parallel interleaved legs of the corresponding phase. For example, as shown in Fig. 1, CI suppresses the circulating current across interleaved legs of the Phase A. Many different pulsewidth modulation (PWM) strategies [1]–[5] have been proposed for CI-based system to suppress the circulating current across interleaved legs of corresponding phase.

The CMI-based system equips each converter with a CMI, as shown in Fig. 1. The CMI suppresses the zero-sequence circulating current (ZSCC) across the two parallel converters [6]–[15]. Besides, the CMI also suppresses the common mode (CM) noise. This article focuses on the CMI-based system. The control approach for CMI-based two parallel converters are classified into two basic architectures: decentralized control and centralized control. The decentralized system includes two independent controllers, where the primary issue is the asynchronous carriers of two controllers, and the research focus on control strategies to synchronize the two carriers [6]–[8]. The centralized architecture does not suffer from asynchronous carriers, and research [9]–[15] focuses on the optimization of vector sequences for key indicators, such as line-current ripple, ZSCC, and common-mode voltage (CMV), as shown in Table I.

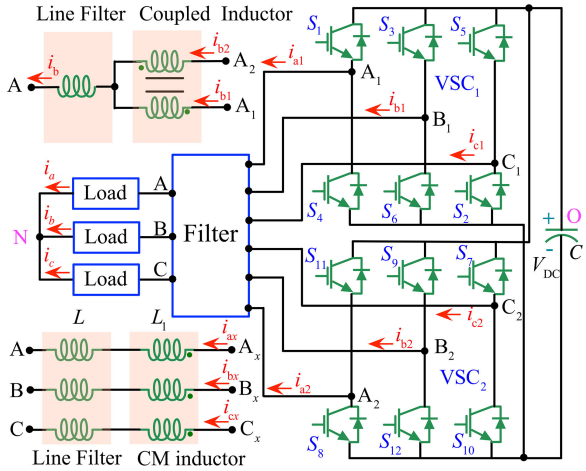

Fig. 1. Two paralleled interleaved inverters with a common dc-link. The filter configuration for circulating current suppression using CI and CMI is illustrated, where x (= 1, 2) enumerates the two paralleled inverters [11].

The line-current ripple originates from the instantaneous voltage error between the reference voltage and actual output voltages. The voltage-error reductions can improve the line-current ripple, which is essential for power converters. For example, in active power filters, the smaller line-current ripple reduces the size of filter inductors [16] and improves the power density; in motor driving systems, the smaller line-current ripple reduces the torque ripple [17].

The ZSCCs originate from instantaneous CMV differences between the two-parallel converters (VSC_1 and VSC_2 in Fig. 1). The ZSCC reduction therefore amounts to reducing the CMV difference. In practice, there are two indicators for the ZSCC: ZSCC peak I_{cirpeak}, and maximum ZSCC peak I_{cirmax}. The ZSCC peak I_{cirpeak} is the largest ZSCC for certain modulation

Manuscript received September 10, 2019; revised October 30, 2019; accepted November 27, 2019. Date of publication December 7, 2019; date of current version March 13, 2020. Recommended for publication by Associate Editor D. O. Neacsu. *(Corresponding author: Stefan M. Goetz.)*

The authors are with Duke University, Durham, NC 27710 USA (e-mail: zhiyong.zeng@duke.edu; zhongxi.li@duke.edu; stefan.goetz@duke.edu).

Color versions of one or more of the figures in this article are available online at http://ieeexplore.ieee.org.

Digital Object Identifier 10.1109/TPEL.2019.2958878

index, and the maximum ZSCC peak is the largest ZSCC for all modulation indices. While I_{cirmax} determines the size of the CM inductors, I_{cirpeak} indicates the additional conduction loss in the CM inductor and semiconductor devices.

The CMV U_{NO} (see Fig. 1) of the two paralleled converters depends on the transistor states (see Fig. 1), and the sequences of CMV reduction methods exclude the vectors introducing larger CMV.

According to different objectives, the modulation strategies in [9]–[15] can be classified as CMV-reduction methods [9], [10], ZSCC-reduction methods [11]–[14], and line-current ripple minimization strategies [15].

Shen *et al.* and Jiang *et al.* explore relationship between CMV and the vector combinations of two converters, and they exclusively use the vectors with zero CMV [9], [10]. The consequent zero-CM PWM completely eliminates the CMV of two parallel converters. However, the proposed zero-CM PWM method uses the zero-voltage vector formed by $\boldsymbol{V}_{000}$–$\boldsymbol{V}_{111}$ and the resultant largest CMV difference (up to $\pm V_{\mathrm{DC}}$) across two converter introduces the larger I_{cirmax}, demanding large CM inductors. In addition, the vector sequences of zero-CM PWM introduce largest voltage errors between the reference and activated vectors, causing largest line current ripples.

As analyzed in [11]–[14], the vectors formed by $\boldsymbol{V}_{111}$ and $\boldsymbol{V}_{000}$ introduce larger CMV differences across the two parallel converters, resulting in large ZSCCs. Indeed, such combinations are ruled out in state-of-the-art ZSCC-suppression methods: the modified discontinuous PWM (MDPWM) [11], active zero-state PWM (AZSPWM) [12], three-level space vector modulation (3LSVM) [13], and the interleaved carrier phase-shift PWM (ICPSPWM) [14]. The methods in [11]–[14] share the same maximum ZSCC peak, which is much smaller than that of the zero-CM PWM [9], [10] and hybrid space vector modulation (HBSVM) [15]. However, the vector sequences of those ZSCC-suppression methods introduce larger voltage errors, causing larger line current ripples than HBSVM [15]. Although AZSPWM [12] and 3LSVM [11] reduce the CMV of MDPWM ($\pm V_{\mathrm{DC}}/2$) to $\pm V_{\mathrm{DC}}/6$, CMV of AZSPWM, MDPWM, and 3LSVM are larger than that of zero-CM PWM.

As widely reflected in the literature [18], [19], the voltage error between the reference and the vector affects the line-current ripples. The vector plane of the two parallel converter resembles that of the neutral-point-clamped three-level converter (NPC-3L), where the nearest three vectors introduce the minimal voltage error. Mimicking the nearest three vectors scheme of NPC-3L, the hybrid space vector modulation HBSVM [15] divides the first 60° sector into seven small triangles areas, and each triangle uses the nearest three vectors to ensure minimal voltage errors and thus smaller line-current ripple. HBSVM demonstrates a better line-current ripple than the known methods. However, HBSVM includes vectors with CMV differences up to $\pm V_{\mathrm{DC}}$, introducing larger ZSCC peak. In addition, HBSVM has the largest CMV ($\pm V_{\mathrm{DC}}$).

It can be concluded that the PWM methods discussed above [9]–[15] entail a tradeoff between line-current ripples, ZSCCs and CMVs: Zero-CM PWMV has zero CMV while introducing larger ZSCC and line-current ripple; MDPWM, AZSPWM, 3LSVM, and ICPSPWM have the minimal ZSCC peak while causing larger CMVs and line-current ripple; and HBSVM has a better line-current ripple than those of others while introducing larger ZSCCs and CMVs.

The various methods have different typical application. For application prioritizing line-current ripple, it is desirable to suppress the overly large ZSCC of HBSVM while maintaining its optimal line-current ripple, which further reduces the CM size and the semiconductor device loss, and improves system power density.

TABLE I
CRUCIAL INDICATORS COMPARISONS OF EXISTING PWM METHODS

	Current ripples	ZSCC peak	CMV peak
AZSPWM [12]	Largest	Minimum	$\pm V_{DC}/6$
MDPWM [11]	Largest	Minimum	$\pm V_{DC}/2$
ICPSPWM [14]	Largest	Minimum	$\pm V_{DC}/6$
3LSVM [13]	Medium	Minimum	$\pm V_{DC}/6$
HBSVM [15]	Minimum	Largest	$\pm V_{DC}/2$
Zero-CM [9, 10]	Largest	Largest	0

This article presents a method that further reduces the ZSCC of HBSVM while ensuring the optimality of the current ripples. We split the space vector plane according to the principle of the nearest three vectors**.** To reduce ZSCC, we investigate all available vector sequences of the nearest three vectors and propose six optimal vector sequences for each 60° sector. We unify all vector sequences under a carrier-based modulation scheme with the assistance of voltage injections. The injected voltage can be computed by a simple algorithm that allows easy implementation in mainstream microcontrollers. The experimental results validate the feasibility and effectiveness of the proposed method.

II. ZSCC, CMV, AND LINE CURRENT RIPPLES OF TWO PARALLEL CONVERTERS

As shown in Fig. 1, the two parallel converters consist of two three-phase two-level converters, and the paralleled interleaved converter, the equivalent output pole voltages are

$$\begin{cases} u_{\mathrm{AN}} = (u_{\mathrm{A1N}} + u_{\mathrm{A2N}})/2 \\ u_{\mathrm{BN}} = (u_{\mathrm{B1N}} + u_{\mathrm{B2N}})/2 \\ u_{\mathrm{CN}} = (u_{\mathrm{C1N}} + u_{\mathrm{C2N}})/2 \end{cases} \tag{1}$$

where $u_{\mathrm{A}x\mathrm{N}}$, $u_{\mathrm{B}x\mathrm{N}}$, and $u_{\mathrm{C}x\mathrm{N}}$ x (= 1, 2) denote the pole output voltage of each three-phase two level converter

$$\begin{cases} u_{\mathrm{AxN}} = \frac{V_{\mathrm{DC}}}{3}(2S_{\mathrm{ax}} - S_{\mathrm{bx}} - S_{\mathrm{cx}}) \\ u_{\mathrm{BxN}} = \frac{V_{\mathrm{DC}}}{3}(2S_{\mathrm{bx}} - S_{\mathrm{ax}} - S_{\mathrm{cx}}) \\ u_{\mathrm{CxN}} = \frac{V_{\mathrm{DC}}}{3}(2S_{\mathrm{cx}} - S_{\mathrm{ax}} - S_{\mathrm{bx}}) \end{cases} \tag{2}$$

where x (= 1, 2) enumerates the two paralleled inverters, N denotes the neutral point. S_{a1} denotes the switching states of the insulated gate bipolar transistor (IGBT) S_1 (see Fig. 1): when $S_{\mathrm{a1}} = 1$, S_1 is ON; when $S_{\mathrm{a1}} = 0$, S_1 is OFF.

Equation (1) shows that different combinations of the vectors from single converter form basic vectors of the two parallel converters, and Fig. 2(a) and Table II show 19 basic vectors of paralleled converters, which are formed by the eight vectors of the single converter shown in Fig. 2(b). These 19 vectors in Table II form redundancies for the reference voltage synthesis.

The ZSCC originates from the instantaneous CMV difference between the two parallel converters and the ZSCC change rate can be expressed as follows [13]:

$$\frac{di_{\mathrm{cir}}}{dt} = \frac{3(u_{\mathrm{N2O}} - u_{\mathrm{N1O}})}{(L_1 + L_2)} \tag{3}$$

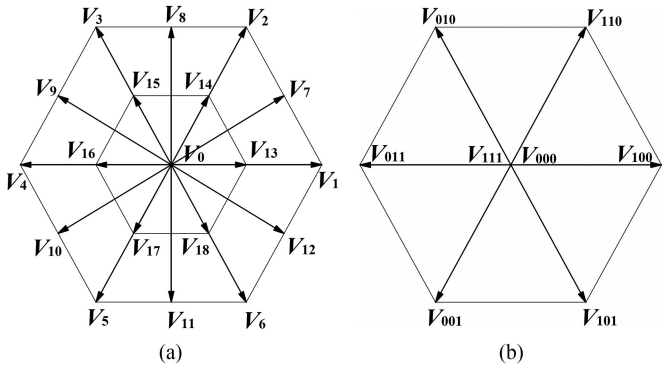

Fig. 2. Space-vector diagram. (a) Two-paralleled converter. (b) Individual converter.

TABLE II
AVAILABLE VOLTAGE VECTORS OF PARALLELED INTERLEAVED CONVERTER

		VSC$_1$							
		V_{000}	V_{100}	V_{110}	V_{010}	V_{011}	V_{001}	V_{101}	V_{111}
VSC$_2$	V_{000}	V_0	V_{13}	V_{14}	V_{15}	V_{16}	V_{17}	V_{18}	V_0
	V_{100}	V_{13}	V_1	V_7	V_{14}	V_0	V_{18}	V_{12}	V_{13}
	V_{110}	V_{14}	V_7	V_2	V_8	V_{15}	V_0	V_{13}	V_{14}
	V_{010}	V_{15}	V_{14}	V_8	V_3	V_9	V_{16}	V_0	V_{15}
	V_{011}	V_{16}	V_0	V_{15}	V_9	V_4	V_{10}	V_{17}	V_{16}
	V_{001}	V_{17}	V_{18}	V_0	V_{16}	V_{10}	V_5	V_{11}	V_{17}
	V_{101}	V_{18}	V_{12}	V_{13}	V_0	V_{17}	V_{11}	V_6	V_{18}
	V_{111}	V_0	V_{13}	V_{14}	V_{15}	V_{16}	V_{17}	V_{18}	V_0

TABLE III
ZSCC CHANGE RATES UNDER DIFFERENT COMBINATION OF VECTORS

		VSC$_1$							
		V_{000}	V_{100}	V_{110}	V_{010}	V_{011}	V_{001}	V_{101}	V_{111}
VSC$_2$	V_{000}	0	-1	-2	-1	-2	-1	-2	-3
	V_{100}	+1	0	-1	0	-1	0	-1	-2
	V_{110}	+2	+1	0	+1	0	+1	0	-1
	V_{010}	+1	0	-1	0	-1	0	-1	-2
	V_{011}	+2	+1	0	+1	0	+1	0	-1
	V_{001}	+1	0	-1	0	-1	0	-1	-2
	V_{101}	+2	+1	0	+1	0	+1	0	-1
	V_{111}	+3	+2	+1	+2	+1	+2	+1	0

where CMV of single converter is

$$u_{\mathrm{NxO}} = \tfrac{1}{3}\left(S_{\mathrm{ax}} + S_{\mathrm{bx}} + S_{\mathrm{cx}}\right) V_{\mathrm{DC}} - \tfrac{1}{2} V_{\mathrm{DC}} \tag{4}$$

and V_{DC} is the dc-link voltage.

With (4) and (3), the ZSCC change rate is

$$\frac{di_{\mathrm{cir}}}{dt} = \frac{V_{\mathrm{DC}}(S_{\mathrm{a2}} + S_{\mathrm{b2}} + S_{\mathrm{c2}} - S_{\mathrm{a1}} - S_{\mathrm{b1}} - S_{\mathrm{c1}})}{(L_1 + L_2)}. \tag{5}$$

Submitting all switching states into (5), we obtain the ZSCC change rates (see Table III) of all vectors, where the change rates are normalized by $V_{\mathrm{DC}}/(L_1 + L_2)$ and with the reference direction from VSC$_2$ to VSC$_1$. Table III also shows the redundancies over ZSCC change rates. For example, $\boldsymbol{V}_0$ can be formed by the pair $\boldsymbol{V}_{000}$–$\boldsymbol{V}_{111}$—which produces the largest change rate, and the pairs $\boldsymbol{V}_{000}$–$\boldsymbol{V}_{000}$—which produces zero change rate. The smaller ZSCC change rates benefit the ZSCC reduction, based on which different ZSCC-reduction methods are proposed [11]–[14].

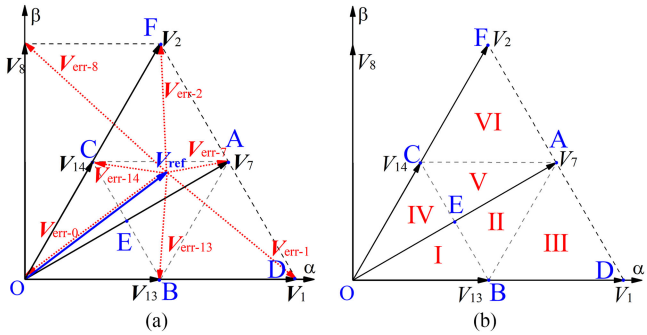

Fig. 3. (a) Vector error illustrations for a given reference voltage $\boldsymbol{V}_{\mathrm{ref}}$. (b) Optimal subsector distribution for the minimal voltage vector errors.

The ZSCC of two parallel converters is as follows:

$$i_{\mathrm{cir}} = i_{\mathrm{a2}} + i_{\mathrm{b2}} + i_{\mathrm{c2}} \tag{6}$$

where i_{a2}, i_{b2}, and i_{c2} are three-phase current of VSC$_2$ (see Fig. 1).

In addition, the CMV u_{NO} of the parallel converter is as follows [9], [10]:

$$\begin{aligned} u_{\mathrm{NO}} &= \tfrac{1}{2}(u_{\mathrm{N1O}} + u_{\mathrm{N2O}}) \\ &= \tfrac{1}{6}\sum_{x=1}^{2}\left(S_{\mathrm{ax}} + S_{\mathrm{bx}} + S_{\mathrm{cx}}\right) V_{\mathrm{DC}} - \tfrac{1}{2} V_{\mathrm{DC}}. \end{aligned} \tag{7}$$

Equation (7) shows that CMV of the two parallel converters depends on the state combination of the two converters, and CMV-reduction methods eliminate the state combinations causing larger CMV when designing the sequences.

The line current ripple originates from the instantaneous voltage error between the reference voltage and the instantaneous output voltage. For example, as shown in Fig. 3(a), there are seven candidate vectors $\boldsymbol{V}_{13}$, $\boldsymbol{V}_7$, $\boldsymbol{V}_{14}$, $\boldsymbol{V}_2$, $\boldsymbol{V}_8$, $\boldsymbol{V}_0$, and $\boldsymbol{V}_1$ in the second 30° sector and the corresponding voltage errors are $\boldsymbol{V}_{\mathrm{err\text{-}13}}$, $\boldsymbol{V}_{\mathrm{err\text{-}7}}$, $\boldsymbol{V}_{\mathrm{err\text{-}14}}$, $\boldsymbol{V}_{\mathrm{err\text{-}2}}$, $\boldsymbol{V}_{\mathrm{err\text{-}8}}$, $\boldsymbol{V}_{\mathrm{err\text{-}0}}$, and $\boldsymbol{V}_{\mathrm{err\text{-}1}}$. Different PWM strategies activate different vectors, resulting in different voltage vector errors and line current ripple. For example, in ΔACE, zero-CM PWM activates $\boldsymbol{V}_8$, $\boldsymbol{V}_7$, and $\boldsymbol{V}_0$ and the voltage vector errors are $\boldsymbol{V}_{\mathrm{err\text{-}8}}$, $\boldsymbol{V}_{\mathrm{err\text{-}7}}$, and $\boldsymbol{V}_{\mathrm{err\text{-}0}}$; HBSVM applies $\boldsymbol{V}_{13}$, $\boldsymbol{V}_7$, and $\boldsymbol{V}_{14}$, where the voltage vector errors are $\boldsymbol{V}_{\mathrm{err\text{-}13}}$, $\boldsymbol{V}_{\mathrm{err\text{-}7}}$, and $\boldsymbol{V}_{\mathrm{err\text{-}14}}$.

Ignoring the parasitic resistance of the filter inductor (L), the line current ripple $\Delta\boldsymbol{i}_{\mathrm{rip}}$ is defined as follows:

$$\begin{aligned} \Delta i_{rip} &= \sqrt{\Delta i_{\mathrm{rip}a}^2 + \Delta i_{\mathrm{rip}b}^2 + \Delta i_{\mathrm{rip}c}^2} \\ &= \sqrt{\frac{3}{2}\left(\Delta i_{\mathrm{rip}\boldsymbol{\alpha}}^2 + \Delta i_{\mathrm{rip}\boldsymbol{\beta}}^2\right)} \\ &= \sqrt{\frac{3}{2}}\sqrt{\left(\frac{\Delta u_{\boldsymbol{\alpha}}}{L}\Delta t\right)^2 + \left(\frac{\Delta u_{\boldsymbol{\beta}}}{L}\Delta t\right)^2} \end{aligned} \tag{8}$$

where $\Delta\boldsymbol{i}_{\mathrm{rip}a}$, $\Delta\boldsymbol{i}_{\mathrm{rip}b}$, and $\Delta\boldsymbol{i}_{\mathrm{rip}c}$ are the current ripple of phase A, phase B, and phase C, respectively; $\Delta\boldsymbol{i}_{\mathrm{rip}\alpha}$ and $\Delta\boldsymbol{i}_{\mathrm{rip}\beta}$ denote the current ripple in the α-axis and β-axis, respectively;

TABLE IV
VECTOR SEQUENCES OF MDPWM, AZSPWM, 3LSVM, ZERO-CM PWM, AND HBSVM IN THE SECOND 30° SECTOR

	Sector IV	Sector V	Sector VI
MDPWM	$V_7(-1) \rightarrow V_2(0) \rightarrow V_0(0)$	$V_7(-1) \rightarrow V_2(0) \rightarrow V_0(0)$	$V_7(-1) \rightarrow V_2(0) \rightarrow V_0(0)$
VSC_1	V_{110} V_{110} V_{111}	V_{110} V_{110} V_{111}	V_{110} V_{110} V_{111}
VSC_2	V_{100} V_{110} V_{111}	V_{100} V_{110} V_{111}	V_{100} V_{110} V_{111}
AZSPWM	$V_0(-1) \rightarrow V_7(+1) \rightarrow V_2(0)$	$V_0(-1) \rightarrow V_7(+1) \rightarrow V_2(0)$	$V_0(-1) \rightarrow V_7(+1) \rightarrow V_2(0)$
VSC_1	V_{101} V_{100} V_{110}	V_{101} V_{100} V_{110}	V_{101} V_{100} V_{110}
VSC_2	V_{010} V_{110} V_{110}	V_{010} V_{110} V_{110}	V_{010} V_{110} V_{110}
3LSVM	$V_0(-1) \rightarrow V_{14}(0) \rightarrow V_7(+1)$	$V_0(-1) \rightarrow V_{14}(0) \rightarrow V_7(+1)$	$V_{14}(0) \rightarrow V_7(+1) \rightarrow V_2(0)$
VSC_1	V_{101} V_{100} V_{100}	V_{101} V_{100} V_{100}	V_{100} V_{100} V_{110}
VSC_2	V_{010} V_{010} V_{110}	V_{010} V_{010} V_{110}	V_{010} V_{110} V_{110}
HBSVM	$V_{14}(+2) \rightarrow V_0(+3) \rightarrow V_{13}(+2) \rightarrow V_{14}(+1)$	$V_{14}(+2) \rightarrow V_7(+1) \rightarrow V_{13}(+2) \rightarrow V_{14}(+1)$	$V_{14}(+2) \rightarrow V_7(+1) \rightarrow V_2(0) \rightarrow V_{14}(+1)$
VSC_1	V_{000} V_{000} V_{100} V_{110}	V_{000} V_{100} V_{100} V_{110}	V_{000} V_{100} V_{110} V_{110}
VSC_2	V_{110} V_{111} V_{111} V_{111}	V_{110} V_{110} V_{111} V_{111}	V_{110} V_{110} V_{110} V_{111}
Zero-CM PWM	$V_0(-3) \rightarrow V_7(-1) \rightarrow V_8(+1) \rightarrow V_0(+3)$	$V_0(-3) \rightarrow V_7(-1) \rightarrow V_8(+1) \rightarrow V_0(+3)$	$V_0(-3) \rightarrow V_7(-1) \rightarrow V_8(+1) \rightarrow V_0(+3)$
VSC_1	V_{111} V_{110} V_{010} V_{000}	V_{111} V_{110} V_{010} V_{000}	V_{111} V_{110} V_{010} V_{000}
VSC_2	V_{000} V_{100} V_{110} V_{111}	V_{000} V_{100} V_{110} V_{111}	V_{000} V_{100} V_{110} V_{111}

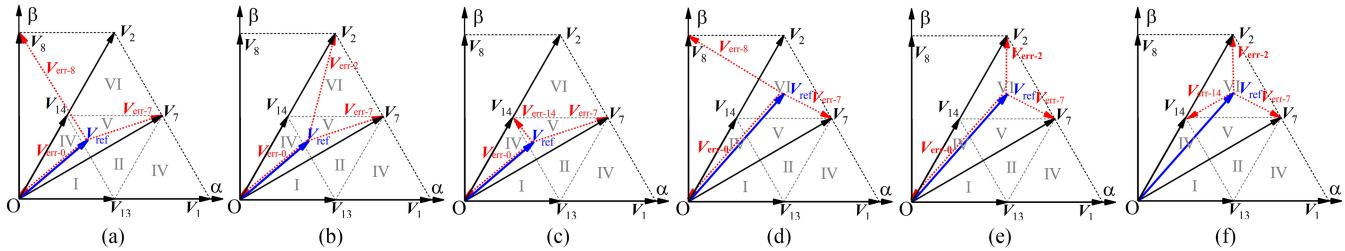

Fig. 4. Voltage vectors errors of (a) Zero CM PWM in Subsector V, (b) AZSPWM/ MDPWM in Subsector V, (c) 3LSVM in Subsector V, (d) Zero CM PWM in Subsector VI, (e) AZSPWM/MDPWM in Subsector VI, and (f) 3LSVM in Subsector VI.

$\Delta \boldsymbol{u}_\alpha$ and $\Delta \boldsymbol{u}_\beta$ are the voltage vector errors in the α-axis and β-axis; and Δt is the time interval.

Equation (8) reveals that the line-current ripple is proportional to the voltage vector errors ($\Delta \boldsymbol{u}_\alpha$ and $\Delta \boldsymbol{u}_\beta$), and the reduced voltage vector error indicates a smaller line current ripple. The space vector plane shown in Fig. 2(a) resembles that of the NPC-3L. As revealed by the current ripple minimization methods of NPC-3L [18], [19], the nearest-three-vector scheme is the optimal solution for minimal voltage vector errors, where each 60° sector of the space vector plane is partitioned into four equilateral triangles and each uses the nearest three vectors. For example, the first 60° sector is partitioned into four equilateral triangles: ΔOCB, ΔBDA, ΔBCA, and ΔFCA [see Fig. 3(b)]. Along with the nearest-three-vector scheme, HBSVM designs the vector sequences using the nearest three vectors, yielding a better line current ripples than that of others.

III. OVERVIEW OF EXISTING PWM METHODS

According to different objectives, the state-of-art modulation strategies can be classified as CMV-reduction methods [9], [10], ZSCC-reduction methods [11]–[14], and line current ripple minimization strategies [15]. This section reviews those PWM strategies mainly from the point of view of voltage vector errors.

Take the second 30° sector for example, which includes Subsectors IV, V, and VI [see Fig. 3(b)]: Table IV shows the vector sequences of MDPWM, AZSWPM, 3LSVM, zero-CM PWM, and HBSVM in Subsectors IV, V, and VI.

In Subsectors IV and V, zero-CM PWM uses three vectors $\boldsymbol{V}_7$, $\boldsymbol{V}_0$, and $\boldsymbol{V}_8$, and the resulting voltage errors $\boldsymbol{V}_{\text{err-7}}$, $\boldsymbol{V}_{\text{err-0}}$, and $\boldsymbol{V}_{\text{err-8}}$, as shown in Fig. 4(a); MDPWM and AZSPWM use three vectors $\boldsymbol{V}_7$, $\boldsymbol{V}_0$, and $\boldsymbol{V}_2$, where the resultant voltage errors are $\boldsymbol{V}_{\text{err-7}}$, $\boldsymbol{V}_{\text{err-0}}$, and $\boldsymbol{V}_{\text{err-2}}$ [see Fig. 4(b)]. The voltage error $\boldsymbol{V}_{\text{err-2}}$ shown in Fig. 4(b) is smaller than $\boldsymbol{V}_{\text{err-8}}$ in Fig. 4(a), reducing the voltage vector errors of the zero-CM PWM.

In Subsectors IV and V, 3LSVM uses three vectors $\boldsymbol{V}_7$, $\boldsymbol{V}_0$, and $\boldsymbol{V}_{14}$ and the consequent voltage errors are $\boldsymbol{V}_{\text{err-7}}$, $\boldsymbol{V}_{\text{err-0}}$, and $\boldsymbol{V}_{\text{err-14}}$ are shown in Fig. 4(c). The voltage vector error $\boldsymbol{V}_{\text{err-14}}$ in Fig. 4(c) is smaller when compared to $\boldsymbol{V}_{\text{err-2}}$ of MDPWM and AZSPWM in Fig. 4(b). Therefore, 3LSVM further reduces the voltage errors of AZSPWM and MDPWM.

In Subsector VI, the resultant voltage errors of zero-CM PWM are $\boldsymbol{V}_{\text{err-7}}$, $\boldsymbol{V}_{\text{err-0}}$, and $\boldsymbol{V}_{\text{err-8}}$, as shown in Fig. 4(d). MDPWM, AZSPWM reduces voltage vector error of zero-CM PWM since $\boldsymbol{V}_{\text{err-2}}$ in Fig. 4(e) is smaller than $\boldsymbol{V}_{\text{err-8}}$ in Fig. 4(d). However, all of them introduce a larger voltage error than that of 3LSVM. As shown in Fig. 4(f), 3LSVM uses the nearest three vector $\boldsymbol{V}_7$, $\boldsymbol{V}_2$, and $\boldsymbol{V}_{14}$ in Subsector VI, which is the optimal solution to the minimal voltage vector errors.

It can be concluded that the 3LSVM reduces the voltage errors of MDPWM and AZSPWM across Subsectors IV, V, and VI. However, the voltage vector errors of 3LSVM is not minimal across the second 30° sector since the nearest three vectors are not obtained in Subsectors IV and V.

Due to the phase shift, the vector sequences and the modulation regions of ICPSPWM are complicated across the space vector plane, so does the voltage vector errors. Therefore, it is unfeasible to compare the voltage vector errors of ICPSPWM to those of others, evaluating its line current ripples. To ensure the integrity of the study, the theoretical analysis and comparisons of the ICPSPWM is performed in Section V.

Table IV shows that HBSVM uses the nearest-three-vector across Subsectors IV to VI: $\boldsymbol{V}_7/\boldsymbol{V}_2/\boldsymbol{V}_{14}$ (Subsector VI), $\boldsymbol{V}_7/\boldsymbol{V}_{13}/\boldsymbol{V}_{14}$ (Subsector V), and $\boldsymbol{V}_{13}/\boldsymbol{V}_0/\boldsymbol{V}_{14}$ (Subsector IV),

TABLE V
OPTIMAL VECTOR SEQUENCES OF SIX SUBSECTORS

Sector I	$V_{13}(0)$	→	$V_0(-1)$	→	$V_{14}(0)$	→	$V_{13}(-1)$	→	$V_0(0)$
VSC_1	V_{101}		V_{101}		V_{100}		V_{100}		V_{000}
VSC_2	V_{110}		V_{010}		V_{010}		V_{000}		V_{000}
Sector II	$V_{13}(0)$	→	$V_7(+1)$	→	$V_{14}(0)$	→	$V_{13}(-1)$		
VSC_1	V_{101}		V_{100}		V_{100}		V_{100}		
VSC_2	V_{110}		V_{110}		V_{010}		V_{000}		
Sector III	$V_{13}(0)$	→	$V_7(+1)$	→	$V_1(0)$	→	$V_{13}(-1)$	→	$V_1(0)$
VSC_1	V_{101}		V_{100}		V_{100}		V_{100}		V_{100}
VSC_2	V_{110}		V_{110}		V_{100}		V_{000}		V_{100}
Sector IV	$V_{14}(0)$	→	$V_0(-1)$	→	$V_{13}(0)$	→	$V_{14}(-1)$	→	$V_0(0)$
VSC_1	V_{100}		V_{101}		V_{101}		V_{111}		V_{111}
VSC_2	V_{010}		V_{010}		V_{110}		V_{110}		V_{111}
Sector V	$V_{14}(0)$	→	$V_7(+1)$	→	$V_{13}(0)$	→	$V_{14}(-1)$		
VSC_1	V_{100}		V_{100}		V_{101}		V_{111}		
VSC_2	V_{010}		V_{110}		V_{110}		V_{110}		
Sector VI	$V_{14}(0)$	→	$V_7(+1)$	→	$V_2(0)$	→	$V_{14}(-1)$	→	$V_2(0)$
VSC_1	V_{100}		V_{100}		V_{110}		V_{111}		V_{110}
VSC_2	V_{010}		V_{110}		V_{110}		V_{110}		V_{110}

which ensures the minimal voltage errors across Subsectors IV, V, and VI. In terms of the voltage vector errors, HBSVM is superior to others. However, the vector sequences of HBSVM include the largest ZSCC change rates of ± 3, introducing largest ZSCC peak. For example, in Subsector IV, according to Table IV, the ZSCC change rates of the vector sequences are $+2 \rightarrow +3 \rightarrow +2 \rightarrow +1$, which accumulates to a large ZSCC. The same applies to other subsectors.

For the application prioritizing the line current ripples, it is desirable to reduce the large ZSCC of HBSVM while maintaining its optimal line current ripples, which reduces the CM inductor size and loss, reduces the semiconductor device loss, and improves system power density.

IV. PROPOSED OPTIMAL LINE CURRENT RIPPLE REDUCTIONS METHODS WITH REDUCE ZSCC

As discussed in Section III, the nearest three vectors are the optimal solution for minimal voltage errors, ensuring the minimal current ripple. Meanwhile, as discussed by the state-of-the-art ZSCC suppression methods, it is essential to maintain the minimal ZSCC change rates to suppress the ZSCC.

To reduce the ZSCC while keeping the current ripple as good as HBSVM, we split the first 60° sector into six subsectors, and each uses the nearest three vectors, as shown in Fig. 3(b). Then, given the redundancy of the vectors, we rule out the vectors with the larger ZSCC change rates, and investigate all available vector sequences of the nearest three vectors with minimal ZSCC change rates, based on which we propose the optimal vector sequences, as shown in Table V.

As revealed by ZSCC suppression method, to reduce the ZSCC peak, the vector sequences should be symmetric across a half-carrier period. Therefore, the proposed sequences are arranged to be symmetric across half-carrier period. Table V only shows the vector sequences of the first quarter of the carrier period. Compared to the ZSCC change rates of HBSVM, the optimal sequences in Table V maintain the minimal ZSCC change rates (± 1). For example, in Subsector I (see Fig. 3) are $0 \rightarrow -1 \rightarrow 0 \rightarrow -1 \rightarrow 0$, whereas the change rates of HBSVM are $+2 \rightarrow +3 \rightarrow +2 \rightarrow +1$.

The optimal switching sequences can be implemented in a carrier-based modulation scheme, as shown in Fig. 5. The switch actions of S_1, S_3, S_5, S_7, S_9, and S_{11}, which determines the vector sequences, are modulated by actions qualified by the comparisons of the carrier and modulation signal. The typical

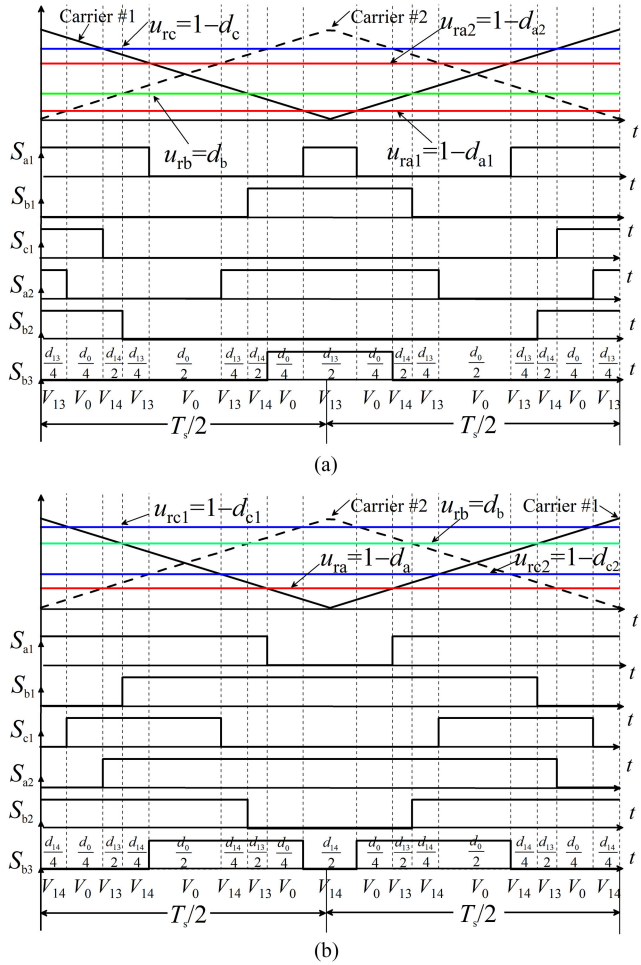

Fig. 5. Vector sequences and the corresponding modulation signals of proposed method in (a) Subsector I and (b) Subsector IV. Carrier #1 and #2 are the carrier of VSC_1 and VSC_2, respectively.

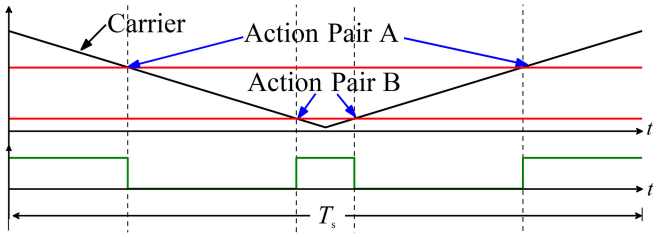

Fig. 6. Two general action pairs qualified by the comparison of the carrier and modulation signal. The two red lines are the modulation signals. Action Pair A: clearing output when modulation signal equals to decreasing carrier; or setting output when modulation signal equals to the increasing carrier. Action Pair B: setting output when modulation signal equals to decreasing carrier; or clearing output when modulation signal amounts to increasing carrier.

actions qualified by the comparison of the carrier and modulation signals are: Action Pair *A* and Action Pair *B*, as shown in Fig. 6.

Fig. 5 shows that different modulation signals are fed with different actions, yielding the optimal vector sequences. For example, in Subsector I [see Fig. 5(a)], modulation single $u_{\rm rb}$ is fed with Action Pair *B*, while and $u_{\rm rc}$ are fed with Action Pair *A*. $u_{\rm ra\text{-}1}$ and $u_{\rm ra\text{-}2}$ are fed with Action Pair *B* and *A*, respectively.

In addition, similar to HBSVM, in each 30° sector, one phase needs to switch twice (two turn-ONS and two turn-OFFS) per carrier period and is therefore equipped with two modulation signals. For example, as shown in Fig. 5(a), in Subsector I, four modulation signals $u_{\rm ra1}$, $u_{\rm ra2}$, $u_{\rm rb}$, and $u_{\rm rc}$ are used, where $u_{\rm ra1}$ and $u_{\rm ra2}$ switch Phase A twice per carrier period; in Subsector IV, $u_{\rm rc1}$ and $u_{\rm rc2}$ switch Phase C twice per carrier period.

Furthermore, it can be found from Fig. 5 that modulation signals equal to either d_x or $(1-d_x)$. For example, in Subsector I, $u_{\rm rb}=d_{\rm b}$ and $u_{\rm rc}=1-d_{\rm c}$. Here, d_x refers to the four duty ratios derived below. Such modification over d_x depends on the activated sector.

To sum up, the implementation of the proposed optimal vector sequences in the carrier-based schemes consists of three sequential steps.

1) calculating the four duty ratios;
2) determining the four modulation signals based on four duty ratios;
3) setting action pair(s) of each modulation signal to yield the optimal vector sequences.

Take Subsectors I and IV as examples to illustrate the implementation of the proposed vector sequences. For Subsectors I and IV [see Fig. 3(b)], three vectors $\boldsymbol{V}_{13}$, $\boldsymbol{V}_{14}$, and $\boldsymbol{V}_0$ are used, and the following expression can be obtain using the voltage-second balancing:

$$\begin{cases} V_{13\boldsymbol{\alpha}}d_{13}+V_{14\boldsymbol{\alpha}}d_{14}=u_{\boldsymbol{\alpha}}=(2u_a-u_b-u_c)/3 \\ V_{14\boldsymbol{\beta}}d_{14}=u_{\boldsymbol{\beta}}=\sqrt{3}(u_b-u_c)/3 \\ d_{13}+d_{14}+d_0=1 \end{cases} \tag{9}$$

where $u_{\rm a}$, $u_{\rm b}$, and $u_{\rm c}$ are the three-phase references; u_α and u_β decompose the references; d_{13}, d_{14}, and d_0 denote the duty ratios of vectors $\boldsymbol{V}_{13}$, $\boldsymbol{V}_{14}$, and $\boldsymbol{V}_0$, respectively; $\boldsymbol{V}_{13\alpha}$ is the α-axis components of $\boldsymbol{V}_{13}$; $\boldsymbol{V}_{14\alpha}$ and $\boldsymbol{V}_{14\beta}$ are the α- and β-axis components of $\boldsymbol{V}_{14}$, respectively.

The solution of (9) is

$$\begin{cases} d_{13}=2\left(u_a-u_b\right)/V_{\rm DC}=2\left(u_a^*-u_b^*\right) \\ d_{14}=2\left(u_b-u_c\right)/V_{\rm DC}=2\left(u_b^*-u_c^*\right) \\ d_0=1+2\left(u_c-u_a\right)/V_{\rm DC}=1+2\left(u_c^*-u_a^*\right) \end{cases} \tag{10}$$

where $u^*{}_{\rm a}$, $u^*{}_{\rm b}$, and $u^*{}_{\rm c}$ are the phase voltage references normalized by $V_{\rm DC}$.

According to the action pairs of four modulation signals and the relationship of modulation signals and duty ratios shown in Fig. 5(a), the following expression is developed:

$$\begin{cases} u_{\rm ra1}=1-d_{\rm a1}=d_{13}/4 \\ u_{\rm ra2}=1-d_{\rm a2}=1/2+d_0/4 \\ u_{\rm rb}=d_b=1/2-d_0/4-d_{13}/4 \\ u_{\rm rc}=1-d_c=1-d_0/4-d_{13}/4 \end{cases} \tag{11}$$

and the four duty ratios can be developed

$$\begin{cases} d_{a1}=1-d_{13}/4=u_a^*+(1-u_c^*/2-2u_a^*) \\ d_{a2}=1/2-d_0/4=u_a^*+(1/4-u_a^*/2-u_c^*/2) \\ d_b=1/2-d_0/4-d_{13}/4=u_b^*+(1/4+u_a^*/2) \\ d_c=d_0/4+d_{13}/4=u_c^*+(1/4+u_a^*/2). \end{cases} \tag{12}$$

TABLE VI
VOLTAGE INJECTIONS OF EACH SUBSECTORS

I, IV	$u^*{}_{\rm m1\text{-}1}=(1+\gamma-4\delta-\tau)/2$	$u^*{}_{\rm m2\text{-}1}=(2-\gamma-2\delta-2\tau)/4$	$u^*{}_{\rm n1}=(2-\gamma+2\delta)/4$
II, V	$u^*{}_{\rm m1\text{-}2}=(2+3\gamma-10\delta)/4$	$u^*{}_{\rm m2\text{-}2}=0.5-\delta$	$u^*{}_{\rm n2}=(2-\gamma+2\delta)/4$
III, VI	$u^*{}_{\rm m1\text{-}3}=(2+\gamma-2\delta+4\tau)/4$	$u^*{}_{\rm m2\text{-}3}=(2-\gamma+2\tau)/4$	$u^*{}_{\rm n3}=0.5-(\delta+\tau)/2$

TABLE VII
FOUR DUTY RATIOS OF SIX SUBSECTORS (THE FIRST 60° SECTOR)

I	$d_{\rm a1}=u^*{}_{\rm a}+u^*{}_{\rm m1\text{-}1}$; $d_{\rm a2}=u^*{}_{\rm a}+u^*{}_{\rm m2\text{-}1}$; $d_{\rm b}=u^*{}_{\rm b}+u^*{}_{\rm n1}$; $d_{\rm c}=u^*{}_{\rm c}+u^*{}_{\rm n1}$
IV	$d_{\rm c1}=u^*{}_{\rm c}+u^*{}_{\rm m1\text{-}1}$; $d_{\rm c2}=u^*{}_{\rm c}+u^*{}_{\rm m2\text{-}1}$; $d_{\rm b}=u^*{}_{\rm b}+u^*{}_{\rm n1}$; $d_{\rm a}=u^*{}_{\rm a}+u^*{}_{\rm n1}$
II	$d_{\rm a1}=u^*{}_{\rm a}+u^*{}_{\rm m1\text{-}2}$; $d_{\rm a2}=u^*{}_{\rm a}+u^*{}_{\rm m2\text{-}2}$; $d_{\rm b}=u^*{}_{\rm b}+u^*{}_{\rm n2}$; $d_{\rm c}=u^*{}_{\rm c}+u^*{}_{\rm n2}$
V	$d_{\rm c1}=u^*{}_{\rm c}+u^*{}_{\rm m1\text{-}2}$; $d_{\rm c2}=u^*{}_{\rm c}+u^*{}_{\rm m2\text{-}2}$; $d_{\rm b}=u^*{}_{\rm b}+u^*{}_{\rm n2}$; $d_{\rm a}=u^*{}_{\rm a}+u^*{}_{\rm n2}$
III	$d_{\rm a1}=u^*{}_{\rm a}+u^*{}_{\rm m1\text{-}3}$; $d_{\rm a2}=u^*{}_{\rm a}+u^*{}_{\rm m2\text{-}3}$; $d_{\rm b}=u^*{}_{\rm b}+u^*{}_{\rm n3}$; $d_{\rm c}=u^*{}_{\rm c}+u^*{}_{\rm n3}$
VI	$d_{\rm c1}=u^*{}_{\rm c}+u^*{}_{\rm m1\text{-}3}$; $d_{\rm c2}=u^*{}_{\rm c}+u^*{}_{\rm m2\text{-}3}$; $d_{\rm b}=u^*{}_{\rm b}+u^*{}_{\rm n3}$; $d_{\rm a}=u^*{}_{\rm a}+u^*{}_{\rm n3}$

Similarly, according to Fig. 5(b), the four duty ratios in Subsector IV are as follows:

$$\begin{cases} d_a=1-d_{14}/4-d_0/4=u_a^*+(3/4+u_c^*/2) \\ d_b=1/2+d_{14}/4+d_0/4=u_b^*+(3/4+u_c^*/2) \\ d_{\rm c1}=d_{14}/4=u_c^*+(-u_a^*/2-2u_c^*) \\ d_{\rm c2}=1/2+d_0/4=u_c^*+(3/4-u_a^*/2-u_c^*/2). \end{cases} \tag{13}$$

Equations (12) and (13) reveal that the four duty ratios contain different signal injections. We further derive the four duty ratios of Subsectors II, III, V, and VI, as listed in Table V. The auxiliary variables a, b, and c are defined as follows:

$$\delta=\begin{cases} u_{\rm max}^*,\ u_{\rm mid}^*\le 0 \\ u_{\rm min}^*,\ u_{\rm mid}^*>0 \end{cases} \quad \tau=\begin{cases} u_{\rm min}^*,\ u_{\rm mid}^*\le 0 \\ u_{\rm max}^*,\ u_{\rm mid}^*>0 \end{cases}$$
$$\gamma=\begin{cases} 1,\ u_{\rm mid}^*\le 0 \\ -1,\ u_{\rm mid}^*>0 \end{cases} \tag{14}$$

where $u^*{}_{\rm max}=\max\{u^*{}_{\rm a}, u^*{}_{\rm b}, u^*{}_{\rm c}\}$; $u^*{}_{\rm min}=\min\{u^*{}_{\rm a}, u^*{}_{\rm b}, u^*{}_{\rm c}\}$; and $u^*{}_{\rm mid}=\text{mid}\{u^*{}_{\rm a}, u^*{}_{\rm b}, u^*{}_{\rm c}\}$.

Table VI shows that with variables defined by (14), the signal injections are unified in the Subsectors pair I/IV, Subsectors pair II/V, and Subsectors pair III/VI. We use subscript "m1-x" or "m2-x" (x identifies the subsector pairs) to denote the two injection signals for the phase that switches twice; and subscript "nx" denotes the shared injected signals for the other two phases. For example, in Subsector I, Phase A is equipped with two duty ratios, and therefore injected with two voltage signals $u^*{}_{\rm m1\text{-}1}$ and $u^*{}_{\rm m2\text{-}1}$; Phases B and C are injected with the shared signals $u^*{}_{\rm n1}$, as shown in Table VII.

In addition, Table VII shows that four duty ratios depend on the activated subsectors, and each subsector applies the different duty ratios. It is necessary to identify the subsector to facilitate the voltage injection. To identify the subsectors, we study their boundaries. The boundary of Subsectors I–III and IV–VI is as follows [15]:

$$u_b^*=0. \tag{15}$$

If $u^*{}_{\rm b}<0$, the reference is in Subsectors I–III; otherwise, the reference is in Subsectors IV–VI.

The segment EB is the boundary of Subsectors I and II:

$$u_\beta^*=-\sqrt{3}(u_\alpha^*-1/3)\Rightarrow u_a^*-u_c^*=1/2. \tag{16}$$

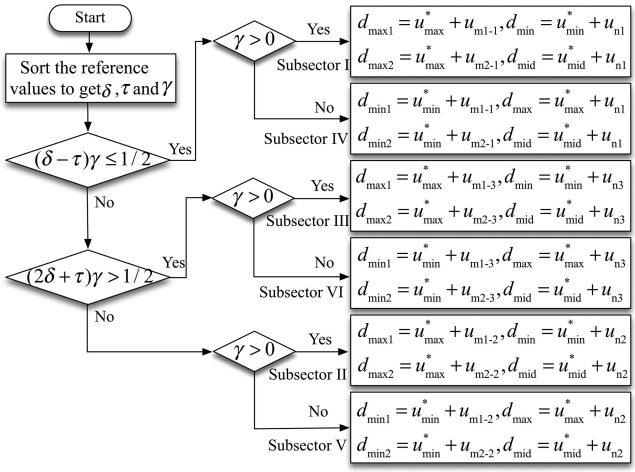

Fig. 7. Procedure of determining the four duty ratios.

The segment AB is the boundary of Subsectors II and III:

$$u^*_\beta = \sqrt{3}(u^*_\alpha - 1/3) \Rightarrow 2u^*_a + u^*_c = 1/2. \tag{17}$$

When $u^*{}_{\rm b} < 0$, if $u^*{}_{\rm a} - u^*{}_{\rm c} < 1/2$, the reference is in Subsector I; if $2u^*{}_{\rm a} + u^*{}_{\rm c} > 1/2$, the reference is in Subsector III; otherwise, the reference is in Subsector II.

The segment AC is the boundary of Subsectors V and VI

$$u^*_\beta = \sqrt{3}/6 \Rightarrow u^*_a + 2u^*_c = -1/2. \tag{18}$$

The segment CE is the boundary of Subsectors IV and V

$$u^*_\beta = -\sqrt{3}(u^*_\alpha - 1/3) \Rightarrow u^*_a - u^*_c = 1/2. \tag{19}$$

When $u^*{}_{\rm b} > 0$, if $u^*{}_{\rm a} - u^*{}_{\rm c} < 1/2$, the reference is in Subsector IV; if $u^*{}_{\rm a} + 2u^*{}_{\rm c} < -1/2$, the reference is in Subsector VI; otherwise, the reference is in Subsector V.

With (15)–(19), it is convenient to identify the subsector to inject the signals across the first 60° sector, determining the four duty ratios. We further explore the boundaries of the six subsectors of the remaining 60°–360° sector, and with the variable defined by (14), the boundary conditions of six subsectors are unified across the entire space vector plane.

The variable $\gamma > 0$ indicates Subsectors I–III, or IV–VI otherwise. Equations (16) and (19) are unified and the boundary of Subsector pair I/IV and Subsector pair II/V is as follows:

$$(\delta - \tau)\gamma = 1/2. \tag{20}$$

Equations (17) and (18) are unified and the boundary of Subsector III/VI and Subsector II/V is as follows:

$$(2\delta + \tau)\gamma = 1/2. \tag{21}$$

With (20), (21), and variable γ, it is convenient to identify the subsectors across the entire space vector plane, as shown in Fig. 7. If $\gamma(\delta - \tau) < 1/2$, the reference is in Subsector pair I/IV; if $\gamma(2\delta + \tau) > 1/2$, the reference is in Subsector pair III/ VI; otherwise, the reference is in Subsector pair II/V. In addition, $\gamma > 0$ indicates Subsectors I–III, or IV–VI otherwise. As such, the combination of $\gamma > 0$ and $\gamma(2\delta + \tau) > 1/2$ picks Subsector III; $\gamma < 0$ and $\gamma(2\delta + \tau) > 1/2$ picks Subsector VI, as shown in Fig. 7.

Using the similar method, we derive on the four duty ratios in remaining 60°–360° sector, based on which we organize the sector identification and the corresponding four duty ratios calculation across the entire plane in a flowchart (see Fig. 7). In Fig. 7, $d_{\rm max\text{-}1}, d_{\rm max\text{-}2}, d_{\rm min\text{-}1}, d_{\rm min\text{-}2}$, and $d_{\rm mid}$ are the duty ratios of the phase having the references $u^*{}_{\rm max}$, $u^*{}_{\rm min}$, and $u^*{}_{\rm mid}$. The phase having the maximum or minimal reference needs two duty ratios to switch twice, which are denoted by $d_{\rm max\text{-}1/2}$ or $d_{\rm min\text{-}1/2}$. For example, in first 60° sector, $u^*{}_{\rm max} = u^*{}_{\rm a}$, $u^*{}_{\rm min} = u^*{}_{\rm c}$, and $u^*{}_{\rm mid} = u^*{}_{\rm b}$. According to Fig. 7, when $\gamma(2\delta + \tau) > 1/2$ and $\gamma > 0$ (Subsector III), $u^*{}_{\rm a} = u^*{}_{\rm max}$ and hence phase A is equipped with two modulation signals: $d_{\rm max\text{-}1}$ $(d_{\rm a1}) = u^*{}_{\rm max}(u^*{}_{\rm a}) + u^*{}_{\rm m1\text{-}3}$ and $d_{\rm max\text{-}2}(d_{\rm a2}) = u^*{}_{\rm max}(u^*{}_{\rm a}) + u^*{}_{\rm m2\text{-}3}$; Phase B is equipped with $d_{\rm mid}(d_{\rm b}) = u^*{}_{\rm mid}(u^*{}_{\rm b}) + u^*{}_{\rm n3}$; and Phase C is equipped with $d_{\rm min}(d_{\rm c}) = u^*{}_{\rm min}(u^*{}_{\rm c}) + u^*{}_{\rm n3}$. If $\gamma(2\delta + \tau) > 1/2$ and $\gamma < 0$ (Subsector VI), Phase C is equipped with $d_{\rm c1}(d_{\rm min\text{-}1})$ and $d_{\rm c2}(d_{\rm min\text{-}2})$ since it has the minimal reference, where $d_{\rm min\text{-}1}$ $(d_{\rm c1}) = u^*{}_{\rm min}(u^*{}_{\rm c}) + u^*{}_{\rm m1\text{-}3}$ and $d_{\rm min\text{-}2}(d_{\rm c2}) = u^*{}_{\rm min}(u^*{}_{\rm c}) + u^*{}_{\rm m2\text{-}3}$; Phase B is equipped with $d_{\rm mid}(d_{\rm b}) = u^*{}_{\rm mid}(u^*{}_{\rm b}) + u^*{}_{\rm n3}$; and Phase A is equipped with $d_{\rm max}(d_{\rm a}) = u^*{}_{\rm max}(u^*{}_{\rm a}) + u^*{}_{\rm n3}$.

With Fig. 7, we can easily determine the duty ratios of three-phase across the entire space vector plane. Once the duty ratios of each phase are calculated by the chart flow (see Fig. 7), the next step is to determine the modulation signals of each phase (d_x versus $1 - d_x$). We investigate all the modulation signals of each phase across the entire vector plane. In summary, the modulation signals take the duty ratios d_x except:

1) when $u^*_b > u^*_c$, Phase A takes the complementary part(s);
2) when $u^*_c > u^*_a$, Phase B takes the complementary part(s);
3) when $u^*_a > u^*_b$, Phase C takes the complementary part(s).

For example, as shown in Fig. 6(a), the modulation signals of Phase A are $u_{\rm ra1} = 1 - d_{\rm a1}$ and $u_{\rm ra2} = 1 - d_{\rm a2}$ since $u^*_b > u^*_c$; modulation signal of Phase C is $u_{\rm rc} = 1 - d_{\rm c}$ since $u^*_a > u^*_b$; and final modulation signal for Phase B is $u_{\rm rb} = d_{\rm b}$ since $u^*_c > u^*_a$.

Once the modulation signals of the three phases are obtained, the final step is to set the action pair(s) of the modulation signal(s) of each phase generating the corresponding gate signals for the optimal vector sequences. In summary, for the phase having two modulation signals, if the phase has the maximum reference $u^*{}_x = u^*{}_{\rm max}$, the larger modulation signal is fed with Action Pair *A*, while the smaller one is fed with Action Pair *B*; if the phase has the minimum reference $u^*{}_x = u^*{}_{\rm min}$, the larger modulation signal is fed with Action Pair *B*, while the smaller one is fed with Action Pair *A*. For the phase including only one modulation signal, if $u_{rx} = 1 - d_x$, u_{rx} is fed with Action Pair *A*, otherwise, u_{rx} is fed with Action Pair *B*.

For example, as shown in Fig. 5(a), Phase A reaches the maximum reference ($u^*{}_{\rm a} = u^*{}_{\rm max}$) in Subector I and thus receives two modulation signals $u_{\rm ra1}$ and $u_{\rm ra2}$, where $u_{\rm ra1}$ is fed with Action Pair *B*, while $u_{\rm ra2}$ is fed with Action Pair *A* since $u_{\rm ra2} > u_{\rm ra1}$; the modulation signal $u_{\rm rb}$ of Phase B is fed with Action Pair *B* since $u_{\rm rb} = d_{\rm b}$; $u_{\rm rc}$ is fed with Action Pair *A* since $u_{\rm rc} = 1 - d_{\rm c}$.

Through matching the derived modulation signals with corresponding actions, we can easily implement the proposed opimal vector sequences in a carrier-based scheme.

V. ZSCC and Line Current Ripples Comparisons Between ICPSPWM, HBSVM, and the Proposed Method

According to the review in Section III, HBSVM is superior to zero-CM PWM, MDPWM, AZSPWM, and 3LSVM in terms of the voltage vector errors, yielding the optimal line current ripples. Since both the proposed method and HBSVM maintain the minimal voltage vector errors across the entire space vector

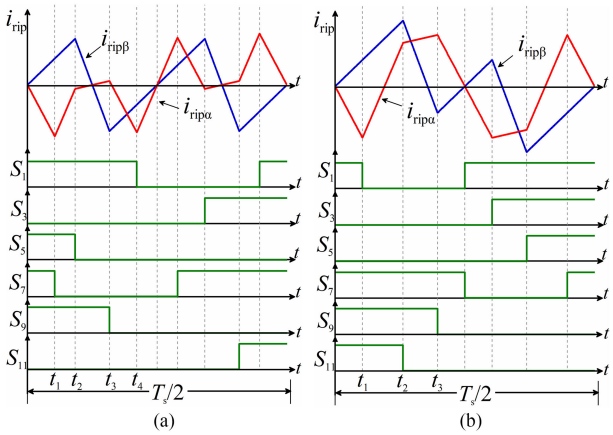

Fig. 8. Line current ripple across half of the carrier period of (a) the proposed method and (b) HBSVM.

plane, it is necessary to quantitatively analyze the line-current ripple of the proposed method and HBSVM. In addition, due to the phase shift, the vector sequences of ICPSPWM and their modulation regions are complicated across the space vector plane. It is unfeasible to compare the voltage vector errors of ICPSPWM to that of others, evaluating the line-current ripple performance of ICPSPWM. Therefore, this section quantitatively analyzes the line-current ripple of the proposed method, ICPSPWM, and HBSVM to validate the merits of the proposed method.

A case study is performed in Subsector I. As shown in Fig. 8, the line-current ripple is symmetric across the half carrier period, where the mean value of the line current ripple is zero across the half carrier period in a stable state, therefore, the line-current ripple analysis can be performed in the first quarter of the carrier period.

According to Fig. 8(a), the line-current ripple of the proposed method consists of five time-integrals of voltage errors in first quarter of the carrier period, which can be expressed as follows:

$$\Delta i_{\mathrm{rip}\alpha}=\begin{cases}\Delta u_{\mathrm{rip}\alpha 0}t/L, & [0,t_1]\\ \Delta u_{\mathrm{rip}\alpha 1}\left(t-t_1\right)/L+\Delta u_{\mathrm{rip}\alpha 0}t_1/L, & [t_1,t_2]\\ \Delta u_{\mathrm{rip}\alpha 2}\left(t-t_2\right)/L+\Delta u_{\mathrm{rip}\alpha 1}\\ \quad\left(t_2-t_1\right)/L+\Delta u_{\mathrm{rip}\alpha 0}t_1/L, & [t_2,t_3]\\ \Delta u_{\mathrm{rip}\alpha 3}\left(t-t_4\right)/L\\ \quad+\Delta u_{\mathrm{rip}\alpha 4}\left(t_4-T_s/4\right)/L, & [t_3,t_4]\\ \Delta u_{\mathrm{rip}\alpha 4}\left(t-T_s/4\right)/L, & [t_4,T_s/4]\end{cases}\tag{22}$$

$$\Delta i_{\mathrm{rip}\beta}=\begin{cases}\Delta u_{\mathrm{rip}\beta 0}t/L, & [0,t_1]\\ \Delta u_{\mathrm{rip}\beta 1}\left(t-t_1\right)/L+\Delta u_{\mathrm{rip}\beta 0}t_1/L, & [t_1,t_2]\\ \Delta u_{\mathrm{rip}\beta 2}\left(t-t_2\right)/L+\Delta u_{\mathrm{rip}\beta 1}\\ \quad\left(t_2-t_1\right)/L+\Delta u_{\mathrm{rip}\beta 0}t_1/L, & [t_2,t_3]\\ \Delta u_{\mathrm{rip}\beta 3}\left(t-t_4\right)/L\\ \quad+\Delta u_{\mathrm{rip}\beta 4}\left(t_4-T_s/4\right)/L, & [t_3,t_4]\\ \Delta u_{\mathrm{rip}\beta 4}\left(t-T_s/4\right)/L, & [t_4,T_s/4]\end{cases}\tag{23}$$

where $\Delta\boldsymbol{i}_{\mathrm{rip}\alpha}$ and $\Delta\boldsymbol{i}_{\mathrm{rip}\beta}$ denote the current ripple in the α-axis and β-axis, respectively.

$\Delta\boldsymbol{u}_{\mathrm{rip}\alpha 0}$–$\Delta\boldsymbol{u}_{\mathrm{rip}\alpha 4}$ in (22) are the voltage errors of α-axis introduced by vector sequences

$$\begin{cases}\Delta u_{\mathrm{rip}\boldsymbol{\alpha}0}=u_{\boldsymbol{\alpha}}-V_{13\boldsymbol{\alpha}}=u_{\boldsymbol{\alpha}}-V_{\mathrm{DC}}/3\\ \Delta u_{\mathrm{rip}\boldsymbol{\alpha}1}=u_{\boldsymbol{\alpha}}-V_{0\boldsymbol{\alpha}}=u_{\boldsymbol{\alpha}}\\ \Delta u_{\mathrm{rip}\boldsymbol{\alpha}2}=u_{\boldsymbol{\alpha}}-V_{14\boldsymbol{\alpha}}=u_{\boldsymbol{\alpha}}-V_{\mathrm{DC}}/6\\ \Delta u_{\mathrm{rip}\boldsymbol{\alpha}3}=u_{\boldsymbol{\alpha}}-V_{13\boldsymbol{\alpha}}=u_{\boldsymbol{\alpha}}-V_{\mathrm{DC}}/3\\ \Delta u_{\mathrm{rip}\boldsymbol{\alpha}4}=u_{\boldsymbol{\alpha}}-V_{0\boldsymbol{\alpha}}=u_{\boldsymbol{\alpha}}.\end{cases}\tag{24}$$

$\Delta\boldsymbol{u}_{\mathrm{rip}\beta 0}$–$\Delta\boldsymbol{u}_{\mathrm{rip}\beta 4}$ in (23) are the voltage errors of β - axis introduced by vector sequences

$$\begin{cases}\Delta u_{\mathrm{rip}\boldsymbol{\beta}0}=u_{\boldsymbol{\beta}}-V_{13\boldsymbol{\beta}}=u_{\boldsymbol{\beta}}\\ \Delta u_{\mathrm{rip}\boldsymbol{\beta}1}=u_{\boldsymbol{\beta}}-V_{0\boldsymbol{\beta}}=u_{\boldsymbol{\beta}}\\ \Delta u_{\mathrm{rip}\boldsymbol{\beta}2}=u_{\boldsymbol{\beta}}-V_{14\boldsymbol{\beta}}=u_{\boldsymbol{\beta}}-\sqrt{3}V_{\mathrm{DC}}/6\\ \Delta u_{\mathrm{rip}\boldsymbol{\beta}3}=u_{\boldsymbol{\beta}}-V_{\mathbf{13}\boldsymbol{\beta}}=u_{\boldsymbol{\beta}}\\ \Delta u_{\mathrm{rip}\boldsymbol{\beta}4}=u_{\boldsymbol{\beta}}-V_{0\boldsymbol{\beta}}=u_{\boldsymbol{\beta}}\end{cases}\tag{25}$$

and t_1, t_2, t_3, and t_4 are

$$\begin{cases}t_1=d_{13}T_s/8\\ t_2=d_{13}T_s/8+d_{14}T_s/4\\ t_3=d_{13}T_s/8+d_{14}T_s/4+d_0T_s/8\\ t_4=d_{13}T_s/4+d_{14}T_s/4+d_0T_s/8\end{cases}\tag{26}$$

where d_{13}, d_{14}, and d_0 are calculated by (10).

The carrier period-based root mean square (rms) of the line current ripple $I_{\mathrm{ripRMS\text{-}Ts}}$ is an indicator of evaluating the current ripple

$$\begin{aligned}I_{\mathrm{ripRMS-Ts}}&=\sqrt{\frac{4}{T_s}\int_0^{\frac{T_s}{4}}\Delta i_{\mathrm{rip}}^2dt}\\ &=\sqrt{\frac{4}{T_s}\int_0^{\frac{T_s}{4}}\frac{3}{2}\left(\Delta i_{\mathrm{rip}\boldsymbol{\alpha}}^2+\Delta i_{\mathrm{rip}\boldsymbol{\beta}}^2\right)dt}.\end{aligned}\tag{27}$$

Submitting (22)–(26) into (27) yields the carrier period-based line-current ripple rms $I_{\mathrm{ripRMS\text{-}Ts}}$

$$\begin{aligned}I_{\mathrm{ripRMS-Ts}}(M,\boldsymbol{\theta})=&\frac{\sqrt{6}MV_{\mathrm{DC}}T_s}{192L}[(36\cos^4\boldsymbol{\theta}-45\cos^2\boldsymbol{\theta}\\ &+36)M^2+(34\sqrt{3}\cos^2\boldsymbol{\theta}\sin\boldsymbol{\theta}-18\cos^3\boldsymbol{\theta}-25\sqrt{3}\sin\boldsymbol{\theta}\\ &-18\cos\boldsymbol{\theta})M-6\sqrt{3}\cos\boldsymbol{\theta}\sin\boldsymbol{\theta}-6\cos^2\boldsymbol{\theta}+18]^{1/2}.\end{aligned}\tag{28}$$

The deduction in Subsector IV shows that the expression of $I_{\mathrm{ripRMS\text{-}Ts}}$ in Subsectors I and IV are identical, which is (28).

The carrier period-based line current ripple rms of HBSVM can be developed using a similar method

$$\begin{aligned}I_{\mathrm{ripRMS-Ts}}(M,\boldsymbol{\theta})=&\frac{\sqrt{6}MV_{\mathrm{DC}}T_s}{192L}[(-72\cos^4\theta\\ &-72\sqrt{3}\cos^3\boldsymbol{\theta}\sin\boldsymbol{\theta}+72\sqrt{3}\cos\boldsymbol{\theta}\sin\boldsymbol{\theta}+36\cos^2\boldsymbol{\theta}\\ &+63)M^2+(64\sqrt{3}\cos^2\boldsymbol{\theta}\sin\boldsymbol{\theta}+144\cos s^3\boldsymbol{\theta}\\ &-64\sqrt{3}\sin\boldsymbol{\theta}-180\cos\boldsymbol{\theta})M-48\cos^2\boldsymbol{\theta}+60]^{1/2}.\end{aligned}\tag{29}$$

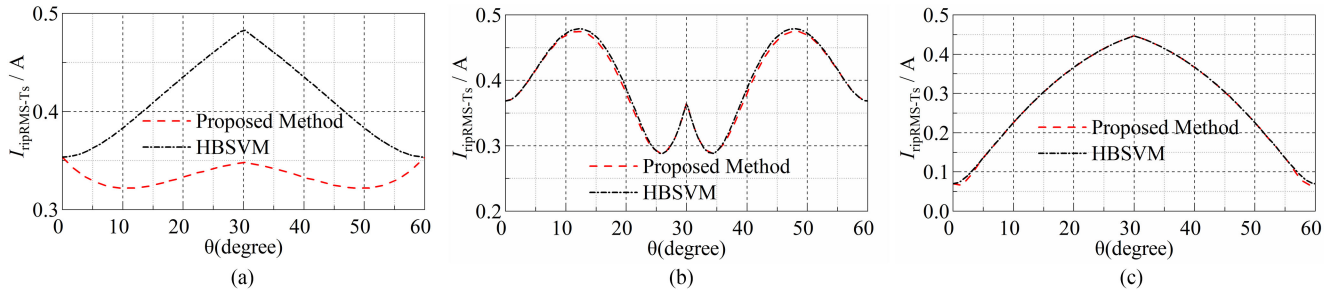

Fig. 9. Carrier period-based line current ripples rms comparisons of the proposed and HBSVM. (a) $M = 0.4$. (b) $M = 0.7$. (c) $M = 1.0$.

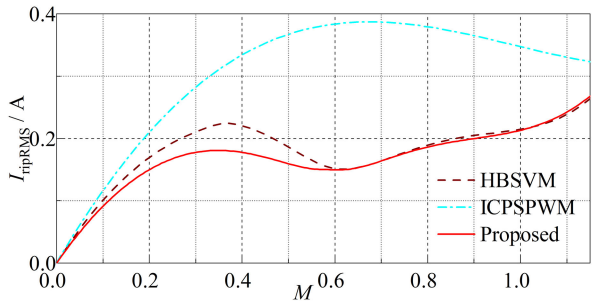

Fig. 10. Fundamental period-based line current ripples rms comparisons between proposed method, HBSVM and ICPSPWM. The carrier periods of the three strategies are adjusted to match the effective switching frequency.

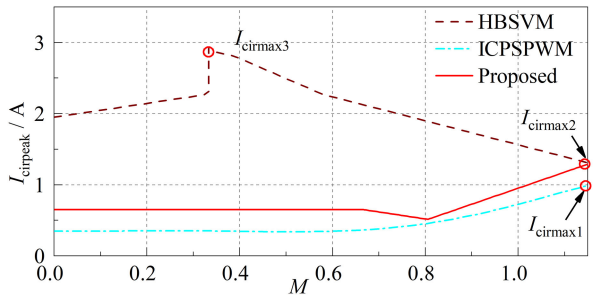

Fig. 11. ZSCC peak comparisons between proposed and existing PWM strategies, where the ZSCC is normalized by $V_{\text{DC}}T_s/(4(L_1+L_2))$. The carrier periods of the three strategies are adjusted to match the effective switching frequency.

Using this similar method, we derive on the carrier period-based line current ripple rms of the proposed method and HBSVM in Subsectors II–VI. Based on the analysis, Fig. 9(a)–(c) compares $I_{\text{ripRMS-Ts}}$ of the proposed method and HBSVM under $M = 0.4$, $M = 0.7$, and $M = 1.0$, respectively. Fig. 9 confirms that the proposed method has a smaller $I_{\text{ripRMS-Ts}}$ than that of HBSVM under $M = 0.4$ while almost overlapping with HBSVM under $M = 0.7$ and $M = 1.0$.

The fundamental period-based current ripple rms I_{ripRMS} is another indicator to evaluate the overall current ripple performance, which depicts the line current ripple respecting modulation index M

$$I_{\text{ripRMS}} = \sqrt{\frac{1}{2\pi}\int_0^{2\pi} I^2_{\text{ripRMS}-\text{T}_s}\, d\theta} \tag{30}$$

where $I_{\text{ripRMS-Ts}}$ is defined by (27).

TABLE VIII
SYSTEM PARAMETERS

R_L	L_1/ L_2	L_3/ L_4	P
16 Ω	5.2 mH	3 mH	3.5 kW
C	V_{DC}	f_1	f_2
1500 μF	350 V	3.3kHz	2.5kHz

Fig. 10 compares I_{ripRMS} of the proposed method and HBSVM, which confirms that the proposed method maintains as good line current ripple as HBSVM in high modulation regions while further reducing the line current ripple of HBSVM in low modulation regions.

As shown in Fig. 8, HBSVM and the proposed method switch one phase twice (two turn-ONS and two turn-OFFS) per carrier period, and the total switching time are increased to 8. The total switching times of ICPSPWM is 6. To ensure the convinced comparisons, we set carrier periods of HBSVM, ICPSPWM, and the proposed method so that the total switching times of identical time interval is identical (the approximately same switching losses). Then, we calculate the fundamental period-based current ripple rms of ICPSPWM, and the results are shown in Fig. 10, which shows that ICPSPWM has a larger I_{ripRMS} than those of HBSVM and the proposed method.

The ZSCC peak is the maximum of ZSCC under a certain modulation index. We calculate the ZSCC of the proposed method across each subsector, and with comparisons, we obtain the ZSCC peak of the proposed method

$$I_{\text{cirpeak}} = \begin{cases} V_{\text{DC}}T_s/(8(L_1+L_2)), & M \in [0, 2/3] \\ V_{\text{DC}}T_s(-3M/4+1)/ \\ (4(L_1+L_2)), & M \in [2/3, (32\sqrt{3}-24)/39] \\ V_{\text{DC}}T_s(\sqrt{3}M-1)/ \\ (4(L_1+L_2)), & M \in [(32\sqrt{3}-24)/39, 2\sqrt{3}/3]. \end{cases} \tag{31}$$

The ZSCC peak of HBSVM is

I_{cirpeak}

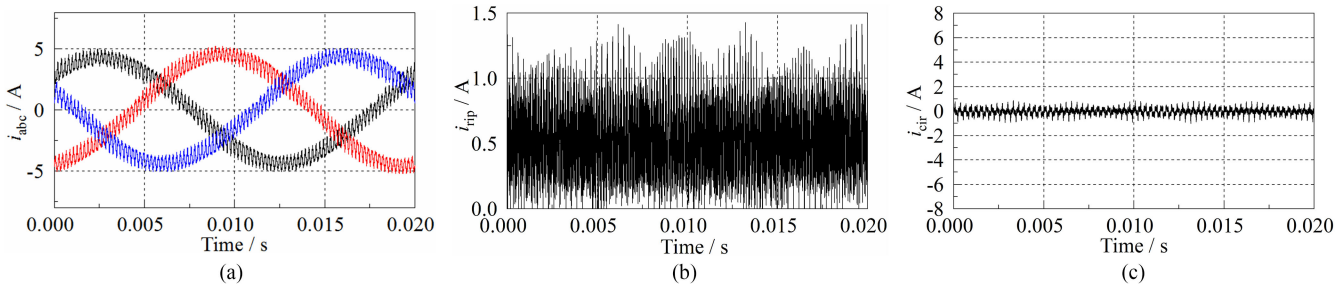

Fig. 12. Experimental results of the ICPSPWM ($f = 3.3$ kHz) under $M = 0.4$. (a) Line current. (b) Line current ripples. (c) ZSCC.

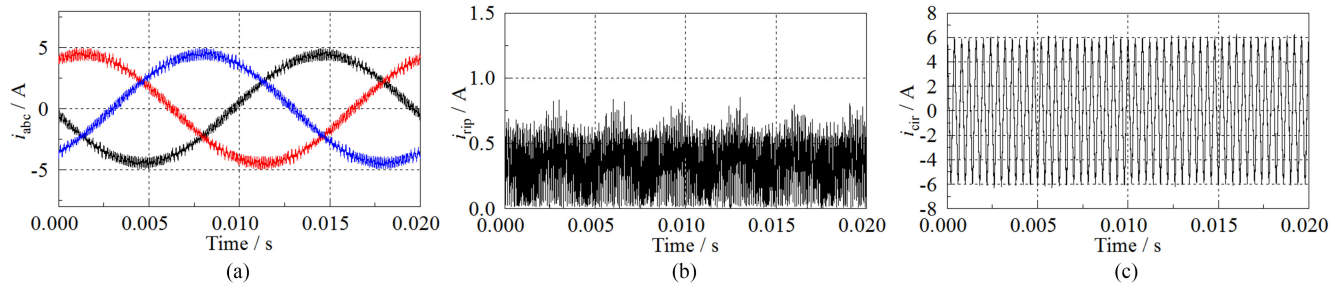

Fig. 13. Experimental results of the HBSVM ($f = 2.5$ kHz) under $M = 0.4$. (a) Line current. (b) Line current ripples. (c) ZSCC.

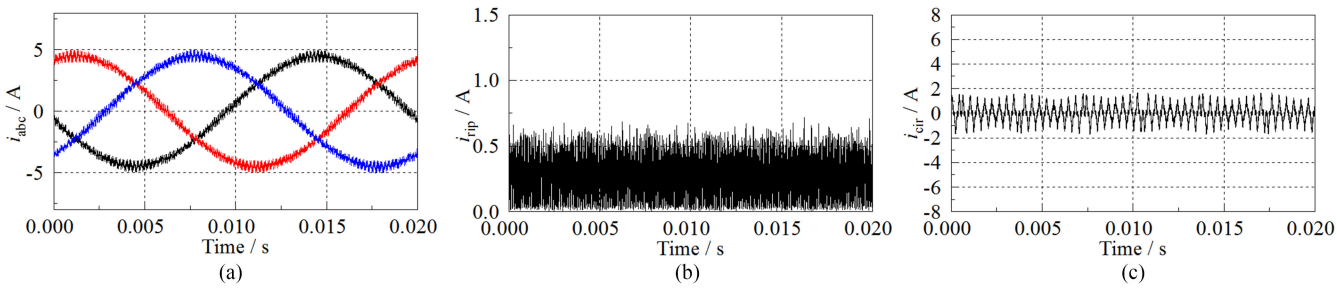

Fig. 14. Experimental results of the proposed method ($f = 2.5$ kHz) under $M = 0.4$. (a) Line current. (b) Line current ripples. (c) ZSCC.

$$= \begin{cases} V_{\mathrm{DC}} T_s (3M+6)/(16(L_1+L_2)), M \subseteq [0, 1/3] \\ V_{\mathrm{DC}} T_s (27 - \sqrt{27M^2 - 3})/(48(L_1+L_2)), \\ \quad M \subseteq [1/3, 2\sqrt{3}/9] \\ V_{\mathrm{DC}} T_s (12 - 5\sqrt{3}M)/(16(L_1+L_2)), \\ \quad M \subseteq [2\sqrt{3}/9, \sqrt{3}/3] \\ V_{\mathrm{DC}} T_s (10 - 3\sqrt{3}M)/(16(L_1+L_2)), \\ \quad M \subseteq [\sqrt{3}/3, 2\sqrt{3}/3]. \end{cases} \tag{32}$$

Fig. 11 compares the ZSCC of HBSVM, ICPSPWM, and the proposed method. Fig. 11 demonstrates that the proposed method significantly reduces the maximum ZSCC peak of HBSVM, minimizing CM inductor size required by HBSVM. In addition, the proposed method maintains a much smaller ZSCC peak than that of HBSVM across the entire modulation region, reducing the loss of the semiconductor and CM inductors. Figs. 10 and 11 confirm that the proposed method significantly reduces the ZSCC peak of HBSVM while maintaining the optimal line current ripples.

Fig. 11 further demonstrates that although the proposed method is categorized as the line current ripple minimization method, the ZSCC of the proposed method is comparable to that of the state-of-art ZSCC suppression method ICPSPWM.

VI. Experiments

An experimental prototype has been constructed to validate the performance of the proposed method. It consists of a TMS320F2808 DSP, a fly-back circuit-based switching power supply board, IGBTs (FF300R17ME4, Infineon), IGBT gate drivers (2SP0115T2C, Concept), current and voltage sensors (LEM), as well as dc-link capacitors (700D158911-590, SBE). The prototype is tested under the inverter mode, whose dc-link is supplied by a three-phase diode rectifier and the ac loads are three resistors (R) and line filter inductor (L_3 and L_4). The CMIs (L_1 and L_2) are added to suppress the high-frequency ZSCC. The parameters are listed in Table VIII.

As discussed in Section IV, to ensure the convinced comparisons, it is essential to set carrier periods of HBSVM, ICPSPWM, and the proposed method so that the total switching times within the same time interval is identical (the approximately same switching losses). The switching frequencies of three methods are set: the proposed method ($f_2 = 2.5$ kHz), ICPSPWM ($f_1 = 3.3$ kHz), and HBSVM ($f_2 = 2.5$ kHz). Then,

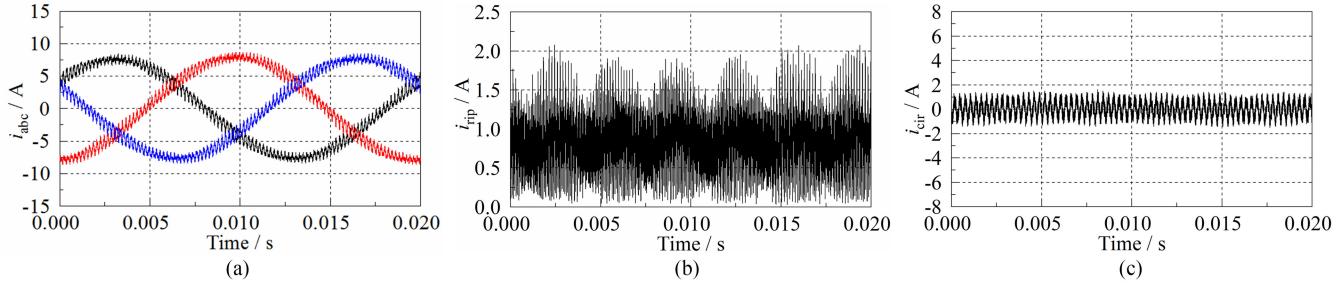

Fig. 15. Experimental results of the ICPSPWM ($f = 3.3$ kHz) under $M = 0.7$. (a) Line current. (b) Line current ripples. (c) ZSCC.

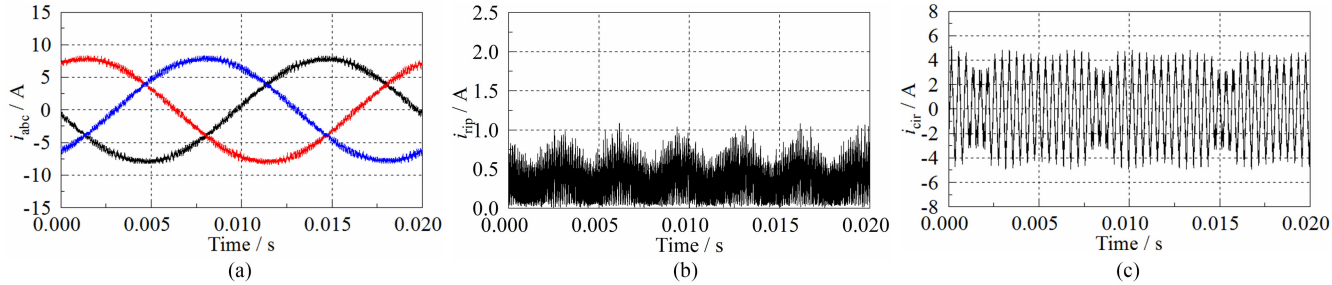

Fig. 16. Experimental results of the HBSVM ($f = 2.5$ kHz) under $M = 0.7$. (a) Line current. (b) Line current ripples. (c) ZSCC.

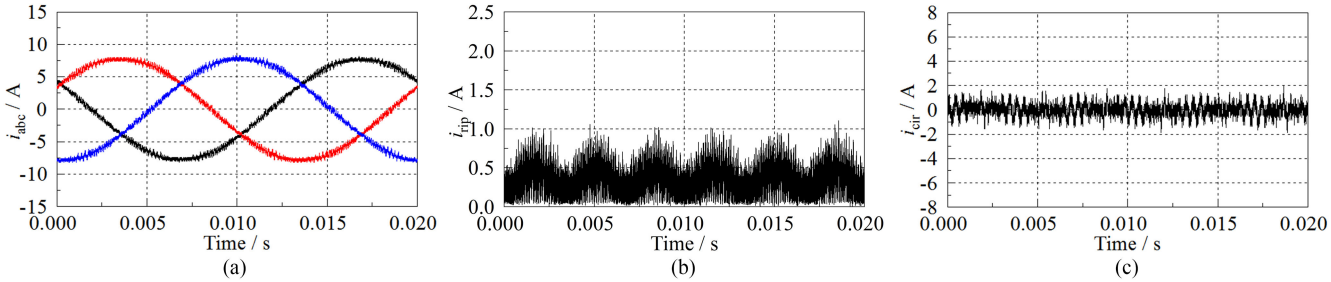

Fig. 17. Experimental results of the proposed method ($f = 2.5$ kHz) under $M = 0.7$. (a) Line current. (b) Line current ripples. (c) ZSCC.

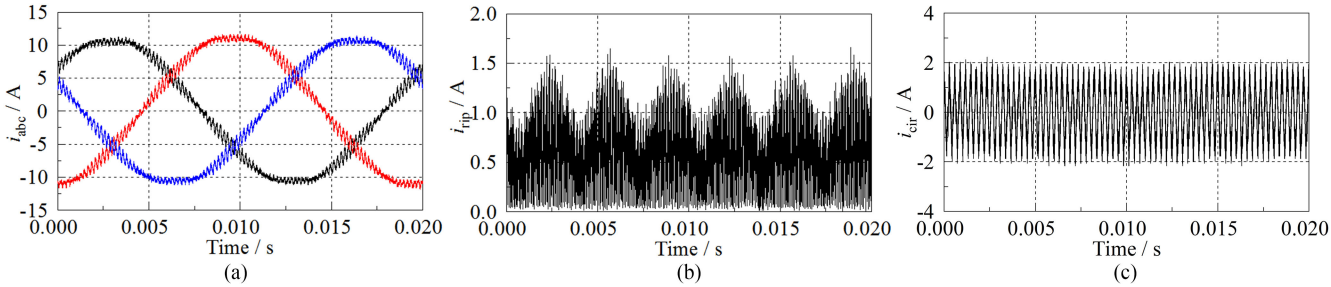

Fig. 18. Experimental results of the ICPSPWM ($f = 3.3$ kHz) under $M = 1.0$. (a) Line current. (b) Line current ripples. (c) ZSCC.

three methods are implemented and tested on the experimental setup with $V_{DC} = 350$ V. To show the effectiveness of the proposed method at a wide modulation region, some typical modulation indices ($M = 0.4$, 0.7, and 1.0) are tested and the line current and the ZSCC are measured. The experimental results are shown in Figs 12–20. Figs. 12–14 show the experimental results at a low modulation index ($M = 0.4$). It is clear the proposed method can effectively reduce the ZSCC of HBSVM while maintaining a better line current ripple. Both the proposed method and HBSVM have a smaller line-current ripple than that of ICPSPWM.

Figs. 15–17 show the experimental results at $M = 0.7$. The experimental results confirm that the line-current ripple of the method is as good as that of HBSVM, which is smaller than that of ICPSPWM. The ZSCC results show that the proposed method significantly reduces the ZSCC of HBSVM. The results shown in Figs. 15–17 confirm the analysis of the current ripple and ZSCC peak in Section VI.

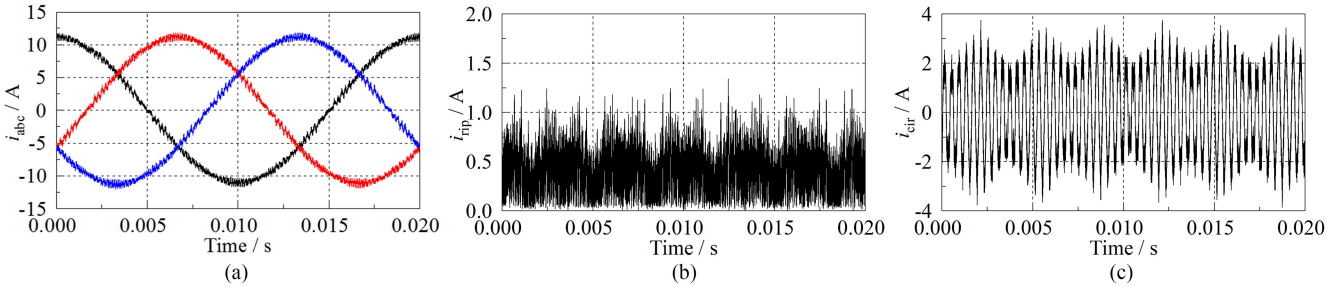

Fig. 19. Experimental results of the HBSVM ($f = 2.5$ kHz) under $M = 1.0$. (a) Line current. (b) Line current ripples. (c) ZSCC.

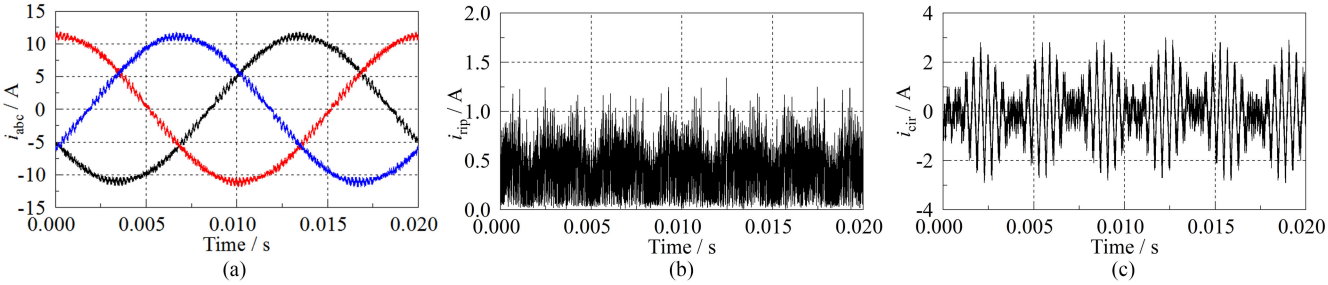

Fig. 20. Experimental results of the proposed method ($f = 2.5$ kHz) under $M = 1.0$. (a) Line current. (b) Line current ripples. (c) ZSCC.

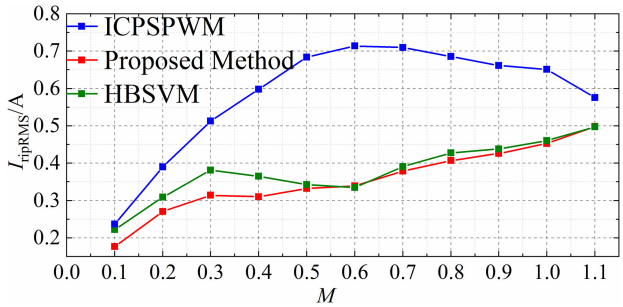

Fig. 21. Line current ripple rms of the three methods. The ICPSPWM are tested with $f = 3.3$ kHz; the proposed method and HBSVM are tested with $f = 2.5$ kHz.

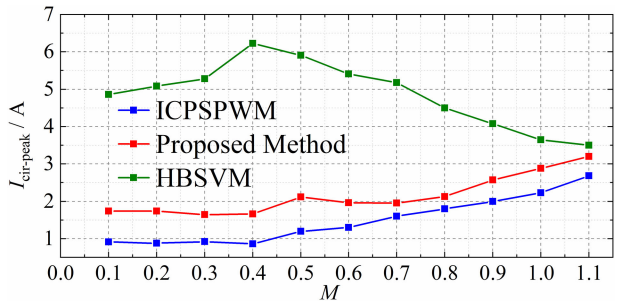

Fig. 22. ZSCC peak of the three methods. The ICPSPWM are tested with $f = 3.3$ kHz; the proposed and HBSVM are tested with $f = 2.5$ kHz.

Figs 18–20 show the experimental results at a high modulation index of $M = 1.0$. The ZSCC results confirm that the proposed method reduces the ZSCC of HBSVM. Meanwhile, the line-current ripples shown in Figs. 18 and 19 are almost the same, and both are smaller to that of ICPSPWM.

To further verify the analysis in Section V, the proposed method, HBSVM, and ICPSPWM are tested in a wide range of modulation index, and the respective ZSCC and line-current ripple are measured. Based on the measurements, we calculate the fundamental-period base-line current ripple rms defined by (30). The experimental results in Fig. 21 clearly show the proposed method maintains the optimal line current ripples across the entire modulation region. Fig. 22 validates that the proposed strategy significantly reduces the ZSCC of HBSVM. The experimental results shown in Figs 12–22 validate that the proposed method further reduces the ZSCC of HBSVM while ensuring the optimality of the current ripples. In addition, although the proposed method is categorized as line current ripple minimization method, the ZSCC of the proposed method is comparable to that of ZSCC suppression method ICPSPWM.

VII. Conclusion

This article introduces a method that further reduces the ZSCC of the existing line current ripple minimization methods while ensuring the optimality of the current ripple. Given the redundancies of the vectors, we propose six optimal vector sequences to reduce the ZSCC of HBSVM. The experimental results validate that the proposed method maintains the minimal line current ripple while significantly reducing the ZSCC of the existing line current ripple minimization methods. In summary, the proposed method is superior to HBSVM since it maintains the minimum line current ripples while further reducing the ZSCC of HBSVM. However, when compared to the state-of-the-art ZSCC peak suppression method, the proposed method still introduces a larger ZSCC. In addition, compared to zero-CM PWM, HBSVM, and

the proposed method suffers from larger CMVs. The proposed method is an ideal PWM method for the application priorities the line current ripples.

REFERENCES

[1] B. Cougo, T. Meynard, and G. Gateau, "Parallel three-phase inverters: Optimal PWM method for flux reduction in intercell transformers," *IEEE Trans. Power Electron.*, vol. 26, no. 8, pp. 2184–2191, Aug. 2011.

[2] J. Ewanchuk and J. Salmon, "Three-limb coupled inductor operation for paralleled multi-level three-phase voltage sourced inverters," *IEEE Trans. Ind. Electron.*, vol. 60, no. 5, pp. 1979–1988, May 2013.

[3] G. J. Capella, J. Pou, S. Ceballos, J. Zaragoza, and V. G. Agelidis, "Current-balancing technique for interleaved voltage source inverters with magnetically coupled legs connected in parallel," *IEEE Trans. Ind. Electron.*, vol. 62, no. 3, pp. 1335–1344, Mar. 2015.

[4] B. Ge, X. Lu, X. Yu, M. Zhang, and F. Z. Peng, "Multiphase-leg coupling current balancer for parallel operation of multiple MW power modules," *IEEE Trans. Ind. Electron.*, vol. 61, no. 3, pp. 1147–1157, Mar. 2014.

[5] G. Gohil, L. Bede, R. Teodorescu, T. Kerekes, and F. Blaabjerg, "Flux-balancing scheme for PD-modulated parallel-interleaved inverters," *IEEE Trans. Power Electron.*, vol. 32, no. 5, pp. 3442–3457, May 2017.

[6] W. Jiang, W. Ma, J. Wang, W. Wang, X. Zhang, and L. Wang, "Suppression of zero sequence circulating current for parallel three-phase grid-connected converters using hybrid modulation strategy," *IEEE Trans. Ind. Electron.*, vol. 65, no. 4, pp. 3017–3026, Apr. 2018.

[7] W. Jiang, Y. Gao, B. Xiao, J. Wang, X. Ding, and L. Wang, "Suppression of high-frequency circulating current caused by asynchronous carriers for parallel three-phase grid-connected converters," *IEEE Trans. Ind. Electron.*, vol. 65, no. 2, pp. 1031–1040, Feb. 2018.

[8] Z. Xueguang, W. Li, Y. Xiao, G. Wang, and D. Xu, "Analysis and suppression of circulating current caused by carrier phase difference in parallel voltage source inverters with SVPWM," *IEEE Trans. Power Electron.*, vol. 33, no. 12, pp. 11007–11020, Dec. 2018.

[9] Z. Shen, D. Jiang, J. Chen, and R. Qu, "Circulating current reduction for paralleled inverters with modified zero-CM PWM algorithm," *IEEE Trans. Ind. Appl.*, vol. 54, no. 4, pp. 3518–3528, Jul./Aug. 2018.

[10] D. Jiang, Z. Shen, and F, "Common-mode voltage reduction for paralleled inverters," *IEEE Trans. Power Electron.*, vol. 33, no. 5, pp. 3961–3974, May 2018.

[11] G. Gohil *et al.*, "Modified discontinuous PWM for size reduction of the circulating current filter in parallel interleaved converters," *IEEE Trans. Power Electron.*, vol. 30, no. 7, pp. 3457–3470, Jul. 2015.

[12] G. Gohil, L. Bede, R. Teodorescu, T. Kerekes, and F. Blaabjerg, "An integrated inductor for parallel interleaved VSCs and PWM schemes for flux minimization," *IEEE Trans. Ind. Electron.*, vol. 62, no. 12, pp. 7534–7546, Dec. 2015.

[13] Z. Quan and Y. W. Li, "A Three-Level space vector modulation scheme for paralleled converters to reduce circulating current and Common-Mode voltage," *IEEE Trans. Power Electron.*, vol. 32, no. 1, pp. 703–714, Jan. 2017.

[14] Z. Quan and Y. W. Li, "Suppressing zero-sequence circulating current of modular interleaved three-phase converters using carrier phase shift PWM," *IEEE Trans. Ind. Appl.*, vol. 53, no. 4, pp. 3782–3792, Jul./Aug. 2017.

[15] K. Shukla, V. Malyala, and R. Maheshwari, "A novel carrier-based hybrid PWM technique for minimization of line current ripple in two parallel interleaved two-level VSIs," *IEEE Trans. Ind. Electron.*, vol. 65, no. 3, pp. 1908–1918, Mar. 2018.

[16] Z. Zeng, W. Zheng, R. Zhao, C. Zhu, and Q. Yuan, "Modeling, modulation, and control of the three-phase four-switch PWM rectifier under balanced voltage," *IEEE Trans. Power Electron.*, vol. 31, no. 7, pp. 4892–4905, Jul. 2016.

[17] Z. Zeng, C. Zhu, X. Jin, W. Shi, and R. Zhao, "Hybrid space vector modulation strategy for torque ripple minimization in three-phase four-switch inverter-fed PMSM drives," *IEEE Trans. Ind. Electron.*, vol. 64, no. 3, pp. 2122–2134, Mar. 2017.

[18] G. Grandi, J. Loncarski, and O. Dordevic, "Analysis and comparison of peak-to-peak current ripple in two-level and multilevel PWM inverters," *IEEE Trans. Ind. Electron.*, vol. 62, no. 5, pp. 2721–2730, May 2015.

[19] T. T. Nguyen, N. Nguyen, and N. R. Prasad, "Novel eliminated common-mode voltage PWM sequences and an online algorithm to reduce current ripple for a three-level inverter," *IEEE Trans. Power Electron.*, vol. 32, no. 10, pp. 7482–7493, Oct. 2017.

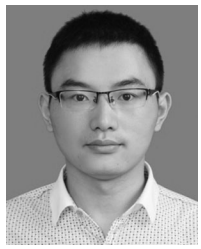

Zhiyong Zeng (M'18) received the Ph.D. degree in electrical engineering from Zhejiang University, Hangzhou, China, in July 2016.

Since September 2016, he has been a Postdoctoral Associate with Duke University, Durham, NC, USA. His research interests include modular pulse synthesizers for transcranial magnetic stimulation, vector sequences optimizations of modular multilevel converters, and fault-tolerant control of grid-connected power converter.

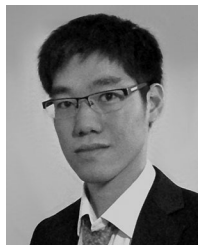

Zhongxi Li (S'17) received the B.S. degree in electrical engineering from Tsinghua University, Beijing, China, in 2015. He is currently working toward the Ph.D. degree with Duke University, Durham, NC, USA.

He was a Visiting Scholar with FREEDM Systems Center, NC State University, where he worked on multilevel converters, and CURENT Engineering Research Center at the University of Tennessee, where he worked on testing wide-band gap semiconductor switches. His research interests include modular pulse synthesizers for magnetic neurostimulation and noninvasive brain stimulation as well as design and control of modular multilevel converters.

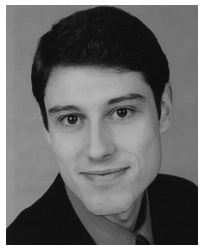

Stefan M. Goetz (M'14) received the undergraduate and graduate degrees from TU Muenchen, Munich, Germany, and the Ph.D. degree in medical applications of power electronics from TU Muenchen.

He obtained doctoral training at TU Muenchen as well as Columbia University. He is currently an Assistant Professor with Duke University, Durham, NC, USA. His research interests include precise high-power pulse synthesizers for magnetic neurostimulation and noninvasive brain stimulation as well as integrative power electronics solutions for microgrids and electric vehicle applications.

Dr. Goetze was awarded a Ph.D. Thesis Prize from TU Muenchen.